AMERICAN SOCIETY FOR MICROBIOLOGY | Applied and Environmental Microbiology®

ENVIRONMENTAL MICROBIOLOGY

Arsenate-Induced Changes in Bacterial Metabolite and Lipid Pools during Phosphate Stress

Weiping Zhuang,[a,b] Narayanaganesh Balasubramanian,[b] Lu Wang,[c] Qian Wang,[c] Timothy R. McDermott,[c] Valérie Copié,[b] Gejiao Wang,[a] Brian Bothner[b]

[a]State Key Laboratory of Agricultural Microbiology, College of Life Science and Technology, Huazhong Agricultural University, Wuhan, China
[b]Department of Chemistry and Biochemistry, Montana State University, Bozeman, Montana, USA
[c]Department of Land Resources and Environmental Sciences, Montana State University, Bozeman, Montana, USA

ABSTRACT *Agrobacterium tumefaciens* GW4 is a heterotrophic arsenite-oxidizing bacterium with a high resistance to arsenic toxicity. It is now a model organism for studying the processes of arsenic detoxification and utilization. Previously, we demonstrated that under low-phosphate conditions, arsenate [As(V)] could enhance bacterial growth and be incorporated into biomolecules, including lipids. While the basic microbial As(V) resistance mechanisms have been characterized, global metabolic responses under low phosphate remain largely unknown. In the present work, the impacts of As(V) and low phosphate on intracellular metabolite and lipid profiles of GW4 were quantified using liquid chromatography-mass spectroscopy (LC-MS) in combination with transcriptional assays and the analysis of intracellular ATP and NADH levels. Metabolite profiling revealed that oxidative stress response pathways were altered and suggested an increase in DNA repair. Changes in metabolite levels in the tricarboxylic acid (TCA) cycle along with increased ATP are consistent with As(V)-enhanced growth of *A. tumefaciens* GW4. Lipidomics analysis revealed that most glycerophospholipids decreased in abundance when As(V) was available. However, several glycerolipid classes increased, an outcome that is consistent with maximizing growth via a phosphate-sparing phenotype. Differentially regulated lipids included phosphotidylcholine and lysophospholipids, which have not been previously reported in *A. tumefaciens*. The metabolites and lipids identified in this study deepen our understanding of the interplay between phosphate and arsenate on chemical and metabolic levels.

IMPORTANCE Arsenic is widespread in the environment and is one of the most ubiquitous environmental pollutants. Parodoxically, the growth of certain bacteria is enhanced by arsenic when phosphate is limited. Arsenate and phosphate are chemically similar, and this behavior is believed to represent a phosphate-sparing phenotype in which arsenate is used in place of phosphate in certain biomolecules. The research presented here uses a global approach to track metabolic changes in an environmentally relevant bacterium during exposure to arsenate when phosphate is low. Our findings are relevant for understanding the environmental fate of arsenic as well as how human-associated microbiomes respond to this common toxin.

KEYWORDS *Agrobacterium tumefaciens* GW4, arsenate, LC-MS/MS, lipidomic, metabolomic

Arsenic is widely present in the earth's crust, occurring naturally in soil, water, and air. In addition to natural geological processes, anthropogenic activities contribute to arsenic found in the environment (1). Arsenic is a known carcinogen and is responsible for several human diseases, including cardiovascular and neurological disorders and diabetes (2). As such, it is ranked first on the U.S. Priority List of Hazardous

Citation Zhuang W, Balasubramanian N, Wang L, Wang Q, McDermott TR, Copié V, Wang G, Bothner B. 2021. Arsenate-induced changes in bacterial metabolite and lipid pools during phosphate stress. Appl Environ Microbiol 87: e02261-20. https://doi.org/10.1128/AEM.02261-20.

Editor Haruyuki Atomi, Kyoto University

Address correspondence to Gejiao Wang, gejiao@mail.hzau.edu.cn, or Brian Bothner, bbothner@.montana.edu.

Received 17 September 2020
Accepted 6 December 2020
Accepted manuscript posted online 23 December 2020
Published 26 February 2021

Substances (Agency for Toxic Substances and Disease Registry [https://www.atsdr.cdc.gov]). Inorganic arsenite [As(III)] and arsenate [As(V)] are the most prevalent chemical species found in the environment. As(III) is more toxic and more mobile than As(V), making it more problematic for natural resource management, mitigation to exposure, and biological assimilation. Microbial transformations are major drivers of this speciation (3) and are important to better understand the mechanisms of arsenic assimilation and toxicity in the environment. Microbe-arsenic interactions have been widely investigated, and the resulting processes are generally classified as mechanisms of arsenic resistance/detoxification or arsenic oxidation as a means of generating cellular energy. Primary arsenic resistance typically consists of As(V) reduction (ArsC) to As(III), which is then extruded (ArsB, Acr3, or ArsK), or arsenic methylation (ArsM) followed by extrusion of methylarsenite (ArsP). As(V) reduction can also occur via action of ArrAB to facilitate anaerobic respiration, whereby As(V) is used as an electron acceptor (1). As(III) can be oxidized to As(V) for either detoxification purposes [as As(V) is less toxic than As(III)] or to generate cellular energy using As(III) as an electron donor for both chemolithotrophic and heterotrophic growth (4–6).

Recent studies have begun to focus on the fate of As(V) when it is taken up by bacteria via phosphate (P_i) transporters. P_i and As(V) are close chemical analogs. Once inside the cell, As(V) can substitute for P_i in various biochemical reactions, some of which contribute to the toxic effects of arsenic: i.e., As(V) substitution for P_i interferes with nucleic acid and ATP synthesis. Alternatively, in work that has thus far primarily focused on marine species, As(V) is known to be incorporated into lipids and sugars (7). Studies on cyanobacteria have provided insights into how bacteria incorporate arsenic into carbon scaffolds, an essential step in synthesizing arsenosugars or arsenolipids (8).

Agrobacterium tumefaciens strains GW4 and 5A respond globally to As(III) at the level of gene transcription (9), protein translation, and cellular metabolism (10, 11). We have also shown that under P_i-limiting conditions, these bacteria gain a growth advantage when provided As(V), possibly due to an ability to incorporate As(V) into lipids (12). As(V) is hypothesized to substitute for P_i for some cell functions, allowing the cell to preserve P_i for essential processes such as nucleic acid synthesis and ATP production, where As(V) substitution is not tolerated (12, 13). The combined metabolomics and lipidomics study reported here addresses a knowledge gap and was undertaken to investigate how As(V) influences the intracellular metabolome and lipid composition of *A. tumefaciens* GW4. Similar to prior studies with As(III) (11), this work reports significant metabolic changes associated with As(V) exposure. Some of the changes in metabolite levels are similar to those reported for *A. tumefaciens* grown in the presence of As(III), whereas others are unique to *A. tumefaciens* growth in the presence of As(V). Most noteworthy, lipid profiles were found to be dramatically altered when *A. tumefaciens* GW4 was grown in the presence of As(V); certain lipids decrease 10- to 50-fold, whereas others increase by up to 15-fold. These observations demonstrate the significant impact of arsenic on cellular growth, deepen our understanding of As(V)'s impact on bacterial metabolism, and fill a knowledge gap about microbe-arsenate (AsV) interactions.

RESULTS

Metabolic response to As(V). Previously, we demonstrated that under phosphate starvation conditions, As(V) can enhance the growth of *A. tumefaciens* GW4 (12). In this study, global metabolite profiles were analyzed to gain insight into the impact of As(V) on the intracellular metabolome of this bacterium. Approximately 1,500 polar features were detected using a hydrophobic interaction liquid chromatography (HILIC) liquid chromatography-mass spectrometry (LC-MS) method in −As(V) and +As(V) sample groups (see Fig. S1 in the supplemental material). A reverse-phase C_{18} liquid chromatography (LC)-MS method revealed approximately 2,600 features in the same samples (Fig. S1). An unsupervised multivariate analysis was performed using principal-

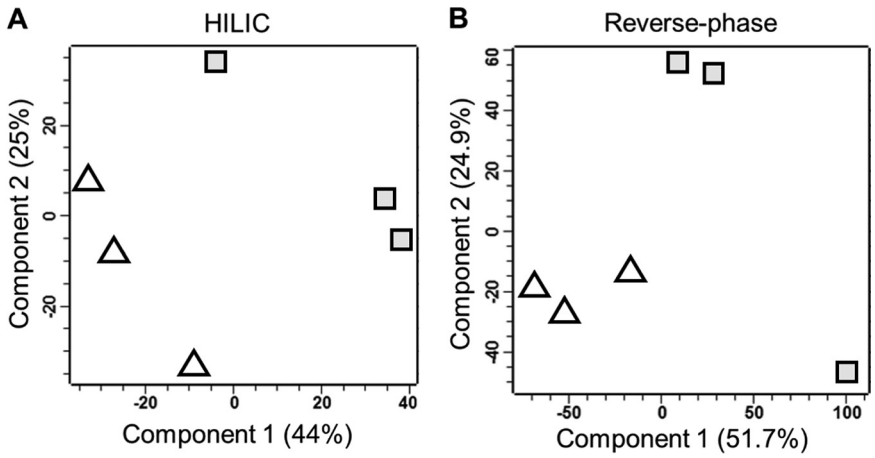

FIG 1 2D-PCA analysis of metabolite profiles obtained from LC-MS. Metabolites were separated using HILIC (A) and reverse-phase (B) chromatography. *A. tumefaciens* GW4 cells were grown in the presence of AsV (squares) separate from the control groups [i.e., no As(V) in the cell culture media] (triangles). The separation is most notable in the first principal-component (PC1) dimension, with PC1 and PC2 accounting for 69 and 77% of the variance between groups for the HILIC and reverse-phase metabolite separation, respectively.

component analysis (PCA) to assess differences in feature abundance (reported as ion intensity) between sample groups. Two-dimensional PCA (2D-PCA) plots of HILIC and reverse-phase LC-MS data sets indicated that ±As(V) groups separate from each other along the first principal-component (PC1) axis, with PC1 and PC2 accounting for a total of 69% of the variance (PC1 = 44% and PC2 = 25%) and 77% (PC1 = 52% and PC2 = 25%) between groups (Fig. 1). Supervised orthogonal partial least-squares discriminant analysis (OPLS-DA) was performed to assess which metabolite pattern changes contributed most to the separation between control and As(V)-treated groups. The 2D OPLS-DA score plots of HILIC and reverse-phase data sets demonstrated that the samples from As(V)-exposed cell cultures are clearly different from the control (see Fig. S2 in the supplemental material), with values of R2Y = 0.99 and Q2 = 0.71 in HILIC data sets and R2Y = 0.99 and Q2 = 0.77 in the reverse-phase data sets, providing high confidence for the OPLS-DA statistical models. Next, an overall comparison between experimental and control groups was undertaken using volcano plots, which revealed that 94 mass spectral features of polar metabolites increased in abundance, while 85 decreased (Fig. 2). A greater number of nonpolar features were found to be altered in reverse-phase LC-MS runs, with 195 nonpolar features increased in abundance and 194 features decreased ($P < 0.05$ and fold change of >1.5).

Metabolic pathways altered by As(V). A total of 42 metabolites were identified based on accurate mass and tandem MS (MS/MS) fragmentation analysis, 12 of which were confirmed by LC retention time matches with authentic standards (see Table S1 in the supplemental material). This group consisted primarily of amino and organic acids. Among the identified metabolites, 21 exhibited significantly different levels between control and As(V)-treated groups ($P < 0.05$, fold change of >1.5), with 17 increased significantly in As(V)-treated cells (Table S1). To identify which metabolite pathways are impacted by As(V), metabolite-level changes were imported into MetaboAnalyst 4.0 and analyzed using the metabolic pathway impact analysis module of MetaboAnalyst. The pathway impact value threshold was set to 0.1, values above which were considered potentially significant impacted pathways. As scores approach 1.0, the confidence that a specific pathway is perturbed increases (14). This analysis highlighted a number of pathways that are significantly impacted by As(V) treatment, including pathways involved in phenylalanine, glutathione, alanine, aspartate,

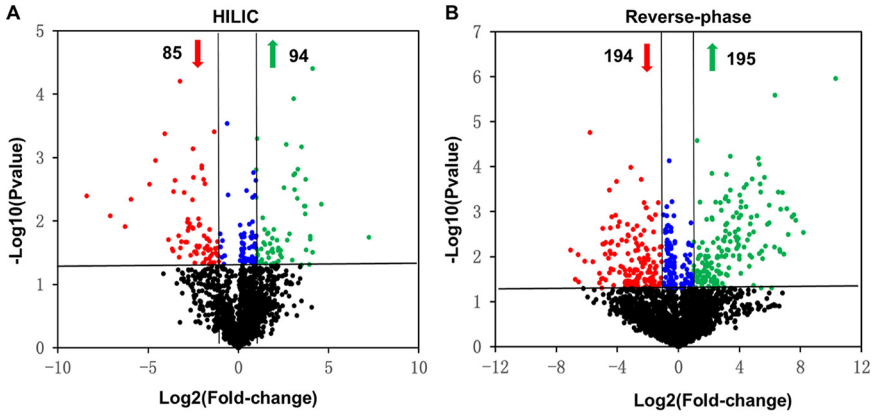

FIG 2 Volcano plots highlighting the distinct metabolite profile differences between the +As(V) *A. tumefaciens* GW4 cells and the −As(V) controls. (A) Volcano plot of MS features identified from the polar HILIC LC-MS analysis, highlighting the 94 and 85 features that are increased and decreased in abundance, respectively, in +As(V) cells. (B) Volcano plot of MS features identified from the nonpolar C_{18} reverse-phase LC-MS analysis, highlighting the 194 and 195 features that are increased and decreased in abundance, respectively, in the +As(V) cells. Horizontal lines indicate a statistical significance *P* value of <0.05. Green and red arrows refer to increase and decrease in abundance, respectively, by >1.5-fold change (FC) and a *P* value of <0.05.

glutamate, vitamin B_6, D-glutamine, histidine, tryptophan, arginine, proline, and pyrimidine metabolism (Fig. 3).

Specific metabolites and impacted pathways were mapped onto KEGG pathways annotated for *Agrobacterium tumefaciens* Ach5 (for which a complete, closed genome sequence is available). The assembled KEGG metabolic network (Fig. 4) revealed that pathway perturbation was primarily reflected in increased metabolite abundance for microbial cells grown in the presence of As(V). Mannitol is the sole carbon source in the $MMNH_4$ medium and enters glycolysis in the form of fructose-6-P, which is eventually converted to pyruvate prior to being further catabolized via the tricarboxylic acid (TCA) cycle and used for oxidative phosphorylation and aerobic cellular energy (ATP) production. Increased activity of these metabolic pathways is consistent with observed increases in malate and succinate levels in As(V)-treated cells (Fig. 4). In addition to

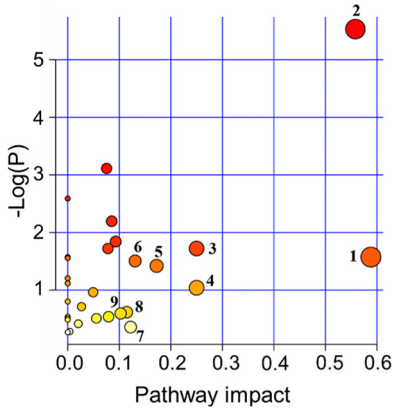

FIG 3 Metabolic pathway impact analysis resulting from *A. tumefaciens* GW4 growth in the presence of arsenate [As(V)]. The plot was generated with MetaboAnalyst 4.0 and KEGG metabolic networks corresponding to *A. tumefaciens* Ach5. Pathways with impact values of ≥0.10 are numbered. Significance ranges from moderate (yellow) to highly significant (red). The size of circles correlates with the number of metabolites that were identified in the LC-MS analysis for each impacted pathway: 1, phenylalanine metabolism; 2, glutathione metabolism; 3, alanine, aspartate, and glutamate metabolism; 4, vitamin B_6 metabolism; 5, D-glutamine and D-glutamate metabolism; 6, histidine metabolism; 7, tryptophan metabolism; 8, arginine and proline metabolism; and 9, pyrimidine metabolism.

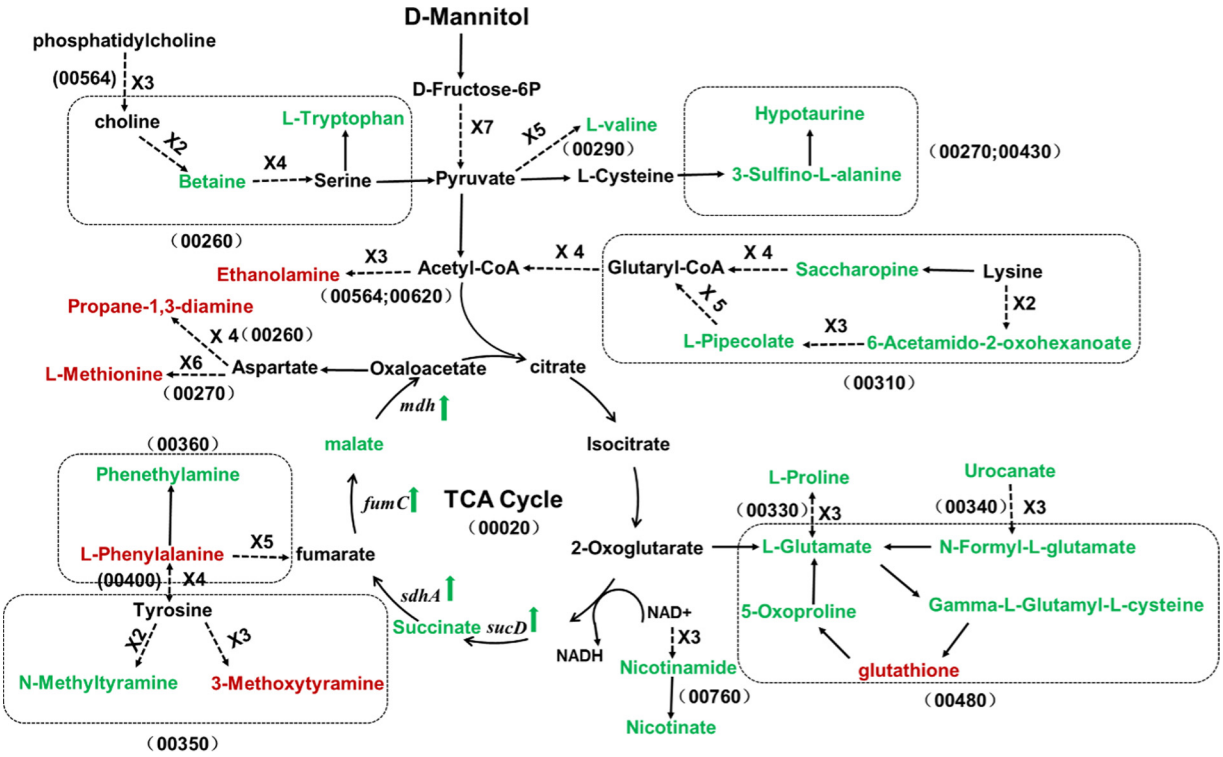

FIG 4 Metabolic network of cellular pathways impacted by As(V). Metabolites were mapped onto KEGG metabolite pathways to show the potential metabolic network based on the reference organism *A. tumefaciens* Ach5. Green text indicates metabolites increased in abundance, red text indicates metabolites decreased in concentration, and black text indicates intermediate metabolites that were not identified by LC-MS. Black dashed arrows indicate pathways that involve more than two intermediates. When more than two intermediates are required, the number of reactions is shown (e.g., X3). Numbers in parentheses refer to the relevant KEGG pathway maps.

increased levels of amino acids, changes in the levels of intermediates involved in the degradation of amino acids were detected. For example, lysine can be degraded via formation of pipecolate and saccharopine intermediates, both of which were higher in abundance in the As(V)-treated *A. tumefaciens* GW4 groups, suggesting that As(V) exposure stimulates lysine catabolism. Metabolites reporting on the redox status of cells, including ethanolamine and reduced glutathione, were less abundant following exposure to As(V), suggesting the presence of a more oxidizing intracellular environment in As(V)-treated cells.

To confirm that gene transcripts of TCA cycle enzymes were altered during growth in the presence of As(V), quantitative PCR (qPCR) was employed to track gene expression of relevant genes. Transcript levels of succinyl coenzyme A (succinyl-CoA) synthetase (*sucD*), succinate dehydratase (*sdhA*), fumarate hydratase (*fumC*), and malate dehydrogenase (*mdh*) were significantly higher by a factor of more than 2-fold (see Fig. S3 in the supplemental material) in As(V)-treated cells, suggesting a significant increase in TCA cycle activity. Enhanced TCA cycle activity also inferred that differences in the energy redox state of the cells may also be taking place. To this end, targeted assays were used to measure intracellular ATP and NADH levels. Cellular ATP and NADH concentrations were approximately 10 nM/cell in cells grown without As(V). In the presence of As(V), ATP increased to greater than 15 nM/cell, whereas no significant change in NADH levels was observed (see Fig. S4 in the supplemental material).

Altered lipid pools in response to As(V). Our previous work revealed that when *A. tumefaciens* GW4 strains are cultured under P_i-limiting conditions, arsenic was detectable in the lipid fraction (12). This led us to conduct a comparative LC-MS analysis of the lipid fractions of *A. tumefaciens* GW4 cells grown with and without As(V). Approximately 1,670 MS lipid features were detected in positive-ion mode and 500 MS features in

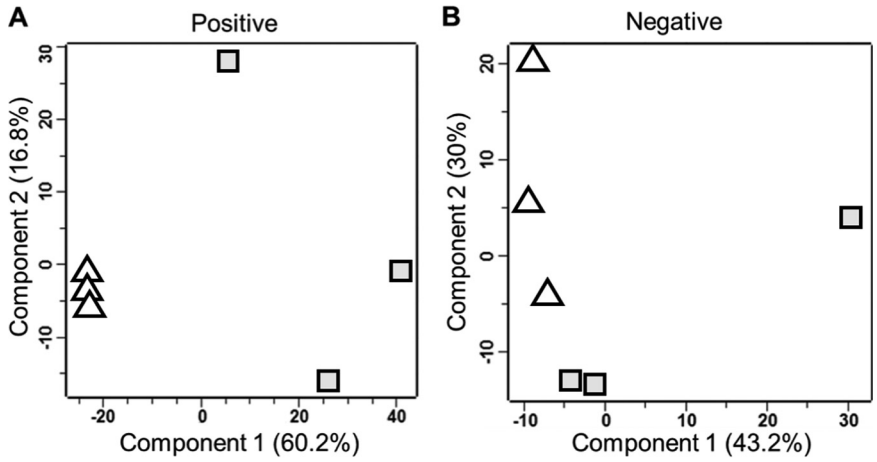

FIG 5 2D-PCA analysis of lipid profiles obtained from LC-MS data. Positive-ion mode (A) and negative-ion mode (B) highlight the separation between *A. tumefaciens* cultures grown in the presence (squares) or absence (triangles) of As(V). The separation is most notable in the first principal-component (PC1) dimension, with PC1 and PC2 accounting for 77 and 73% of the variance between groups in the 2D-PCA plots shown in panels A and B, respectively. The 2D-PCA plots were generated using LC-MS features observed in all samples and amounted to the analyses of 1,670 and 500 MS spectral features for the data shown in panels A and B, respectively.

negative-ion mode (see Fig. S5 in the supplemental material). PCA analysis revealed that −As(V) cultures grouped together and clearly separated from the +As(V) cells based on distinct MS features observed in positive-ion mode, with the first two principal components (PC1 = 60.2% and PC2 = 16.8%) accounting for 77% of the total variance (Fig. 5A). Separation between control and As(V)-treated groups was less evident based on MS spectral features collected in negative-ion mode (Fig. 5B). OPLS-DA was employed to assess which mass spectral features exhibited significant fold changes that contributed most to the separation between As(V)-treated and control groups. The plot of 2D-OPLS-DA scores indicated that the As(V)-exposed groups are clearly different from the control group, with R2Y = 0.99 and Q2 = 0.92 for the lipid feature changes observed in LC-MS positive-ion mode and R2Y = 0.99 and Q2 = 0.91 for those observed in negative-ion mode (see Fig. S6 in the supplemental material). The high values of R2Y and Q2 indicate that As(V) treatments result in significant changes in lipid composition in *A. tumefaciens* strain GW4. Analyses using volcano plots quantified differences between the groups, revealing 375 MS features that were increased in abundance and 125 MS features that were decreased in abundance for the data sets collected in positive-ion mode. In negative mode, 29 MS features increased in abundance and 32 decreased based on P values of <0.05 and fold changes of >1.5 (Fig. 6).

Lipid identification. The significant difference in the lipid composition inspired a deeper look. Lipids were identified using LipidBlast, a reference library of lipids developed using experimental and *in silico* MS/MS fragmentation data (15). Reverse Dot (Rev-Dot) scores were calculated from the experimental MS/MS data using an automated batch search (16). Rev-Dot scores are a measure of similarity between library and experimental spectra weighted for shared ions. Scores range from 0 to 999, with 999 being a perfect match. A cutoff of 600 was used to reduce false-positive matches (16). From this analysis, 74 lipids were identified with a Rev-Dot score of >600 (see Table S2 in the supplemental material). Identified lipids belonging to glycerophospholipid classes included: phosphotidylcholine (PC), phosphatidylethanolamine (PE), phosphatidylglycerol (PG), phosphatidylserine (PS) and phosphatidic acid (PA) (Table S2). In addition, the three minor lipids lysoPE 18:4, lysoPE 18:1, and lysoPC 20:0 were detected in the MS data collected in positive-ion mode. Representative MS/MS data for fragmentation pattern matching demonstrate the high degree of similarity between

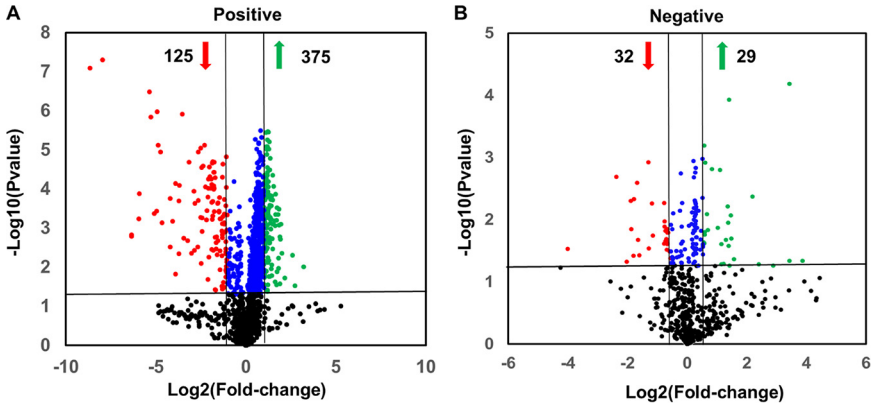

FIG 6 Volcano plots highlighting the lipid profile differences between +As(V) *A. tumefaciens* GW4 cells and −As(V) controls. Volcano plots of LC-MS lipid profiles for *A. tumefaciens* GW4 grown in the presence and absence of As(V). Data were collected in (A) positive- and (B) negative-ion modes. The plots show that 375 features increased and 125 decreased in abundance in positive mode (A), while 29 and 32 features increased and decreased in abundance in negative mode (B). Horizontal lines indicate a statistical significance *P* value of <0.05. Green and red arrows refer to increase and decrease in abundance, respectively, by a >1.5-fold change and a *P* value of <0.05.

experimental and library spectra, even for minor lipid components such as lysoPC 20:0 and lysoPE 18:1 (Fig. 7). Three glycerolipid classes were assigned, corresponding to monoglycosyldiacylglycerol (MGDG), diglycosyldiacylglycerol (DGDG), and triacylglycerol (TG) (Table S2). DGDG 34:1 and MGDG 40:1 exhibited the highest score possible, 999 (see Fig. S7 in the supplemental material).

The properties of glycerophospholipids depend on the chemical nature of their headgroups, which define their lipid class and yield distinctive fragmentation patterns that can be used for classification (17, 18). To take advantage of these features, we cross-checked recorded MS/MS spectra with diagnostic fragmentation patterns reported for glycerophospholipid headgroups. In positive-ionization mode, phosphotidylcholine (PC)-related ions included *m/z* 125 $[M+H]^+$, *m/z* 147 $[M+Na]^+$, and *m/z* 184

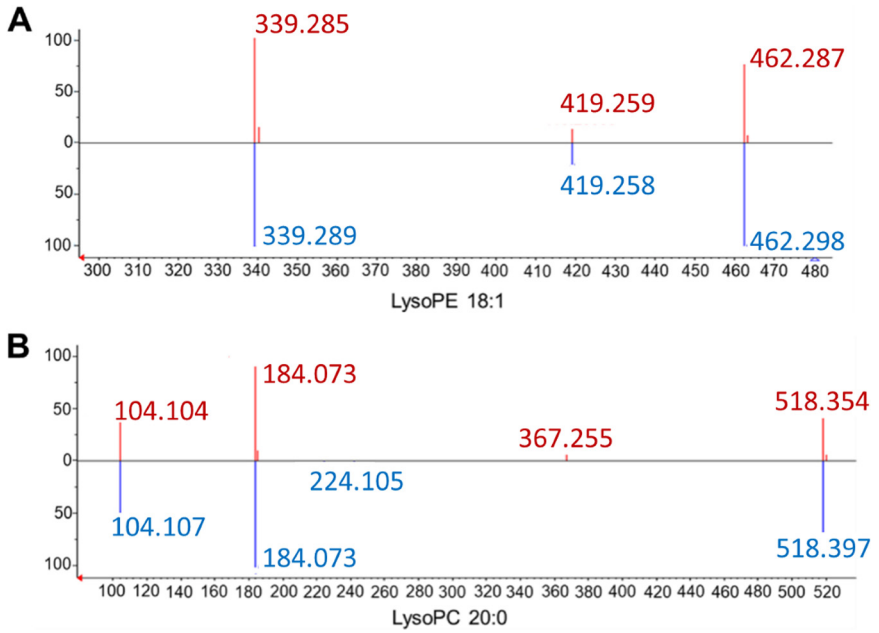

FIG 7 Experimental MS/MS spectra (red) and corresponding matching spectra from the LipidBlast library (blue). (A) LysoPE 18:1 (*m/z* 480.302), with a significance score of 980, and (B) lysoPC 20:0 (*m/z* 536.367), with a significance score of 921.

(protonated phosphatidylcholine). For the phosphatidylethanolamines (PE), the headgroup-associated MS fragments included phosphoric acid $[M+Na]^+$ *m/z* 121 and phosphoethanolamine $[M+Na]^+$ *m/z* 164. The product ions $[M-171]^+$ and $[R_1+116]^+$ were diagnostic for phosphatidylglycerol (PG). In the negative-ion mode, $R_1CH_2COO^-$, $R_2CH_2COO^-$, $[M\text{-}H\text{-}R_2CH{=}C{=}O]^-$ and glycerophosphate ions (*m/z* 153) were used to support these lipid identifications (17). Using this approach, the assignments of 16 glycerophospholipids were validated by matching headgroup fragmentation patterns (see Table S3 in the supplemental material). Overall, a total of 90 lipids could be assigned to specific lipid classes. Of these, 54 lipids were increased in abundance and 36 lipids were decreased in abundance in cells cultured with As(V), with increases up to 14.6-fold and decreases of as much as 50-fold (Table S2 and Table S3). For the identified species, 59 abundance changes were significant, with *P* values of <0.05 and fold changes of >1.5. Significant differences in glycerolipid and glycerophospholipid species were observed, with elevated levels of MGDG, DGDG, TG, and PG and decreased levels of PE, PA, and the three minor lipids lysoPE 18:4, lysoPE 18:1, and lysoPC 20:0, in the As(V)-treated groups.

DISCUSSION

Transcriptomics, proteomics, and metabolomics are being employed to understand microbial global-level responses to arsenic (11, 19–24). However, the majority of these studies have focused on evaluating the effects of arsenite [As(III)]. In contrast, the influence of As(V) on microbial metabolic networks is less understood. This study aids in filling this gap by investigating how bacterial metabolites and lipid compositions change when cells are exposed to As(V). We point out that strain GW4 carries genes for both As(III) oxidation (*aioBA*) and As(V) reduction (*arsC*). It is likely that low basal or induced levels of ArsC act to reduce some of the added As(V), so we cannot completely rule out that some of our observations are a result of limited As(III) production. However, the culture conditions used in this study are well documented to favor As(III) oxidation to As(V), such that the net cell activity of GW4 (and our other model bacterium, *A. tumefaciens* strain 5A) strongly favors As(III) oxidation (6, 25, 26) such that it is not possible to experimentally speciate the arsenic oxyions. Indeed, the only way to detect As(V) reduction is to knock out AioBA activity, which we have done, and that then allows the ArsC activity to be manifested (25). Further, GW4 carries multiple copies of the As(III) extruder Acr3 (10), with the final result being As(III) exported so as to allow for immediate reoxidation to As(V) in the periplasm.

Generation of hydroxyl radical ($^{\bullet}OH$), hydrogen peroxide (H_2O_2), and superoxide anion ($O_2^{\bullet-}$) will damage macromolecules such as DNA, proteins, and lipids. This is one of the mechanisms responsible for the cellular toxicity of arsenic (27, 28), while also inducing the restorative measures of DNA repair and oxidative stress response (29–31). Glutathione plays a central role in oxidative stress detoxification and the maintenance of intracellular redox balance (32). Consistent with these observations, our pathway analysis revealed that glutathione metabolism is altered following *A. tumefaciens* GW4 growth in the presence of As(V) (Fig. 3). Glutamate, 5-oxoproline, and γ-L-glutamyl-L-cysteine are all involved in glutathione metabolism, and their increased levels suggest that glutathione catabolism is upregulated in the As(V)-treated group. The decrease in reduced glutathione suggests that a change in cellular redox potential to a more oxidizing environment has occurred. Under such conditions, DNA repair activities would be expected to increase. The accumulation of nicotinamide supports this inference, as nicotinamide has been reported to reduce arsenic-induced DNA damage and to enhance repair of damaged DNA (33). The increase in tryptophan and altered tryptophan metabolism are also closely related to DNA repair activities. Tryptophan is used in the synthesis of 3-indolepropionic acid, a potent antioxidant used to mitigate DNA damage (34). Increased levels of nicotinamide and tryptophan, along with altered tryptophan-related pathways, allow us to conclude that As(V) exposure requires DNA repair activities in *A. tumefaciens*. Proline, glutamate, hypotaurine, and betaine can also act as

reactive oxygen species (ROS) scavengers, intracellular enzyme protectants, inhibitors of lipid peroxidation, and antioxidants (35–38). The increase in proline, glutamate, hypotaurine, and betaine levels in the As(V)-treated group further supports their role as intracellular protectors of oxidative stress.

Metabolic pathway impact analysis also showed that vitamin B_6 metabolism and its derivative, pyridoxal 5′-phosphate (PLP), are affected (Fig. 3), resulting in significantly increased PLP levels (Table S2). PLP is an important cofactor for enzymes involved in amino acid metabolism, catalyzing transamination, racemization, decarboxylation, and α/β-elimination reactions (39). While vitamin B_6 has a central role in amino acid metabolism, it can also function as a protective agent against ROS (40). The observed increased levels of PLP may thus help ensure amino acid metabolic homeostasis.

Our prior work that examined As(III) metabolic responses employed *A. tumefaciens* strain 5A (11), whereas in the current As(V) study, we elected to use strain GW4 because it incorporates higher levels of arsenic in cellular materials, particularly lipids, with about 0.4 mmol arsenic/g dry weight of pellet incorporated into the polar lipid fraction of *A. tumefaciens* GW4 when exposed to 1 mM As(III) or As(V) (12). Also, since all known documentation of arsenic incorporation into carbon skeletons involves the pentavalent species, the ability of GW4 to oxidize As(III) and to respond to low P_i made it the best choice for this study. Because this study used a different bacterial strain and arsenic species, readers are cautioned on making direct comparisons between regulated metabolites and pathways. For example, the amino acid profile in As(III)-treated cultures showed an impact on amino acid synthesis radiating from pyruvate (11), presumably due to the previously characterized As(III) inhibition of enzymes containing a dihydrolipoamide dehydrogenase subunit, such as pyruvate dehydrogenase (41–43). In contrast, there was little evidence of this occurring in As(V)-exposed GW4 cultures (Fig. 4). It is interesting that the TCA cycle is perturbed in As(V)-treated cells, at both the transcriptional (Fig. S3) and metabolite (Fig. 4) levels, but again was not apparent in As(III)-exposed cultures (11). Similarly, elevated levels of fumarate, succinate, citrate, and glutarate were also reported in green microalga *Scenedesmus* sp. strain IITRIND2 grown in the presence of As(V) (36). When considered in the context of generating cellular energy, it is possible that enhanced TCA cycle activity may have contributed to enhanced ATP levels (Fig. S4), which in turn helps explain As(V)-enhanced growth of P_i-stressed GW4 (12).

The impact of As(V) on lipid metabolism was of particular interest in this study. Glycerophospholipids and glycerolipids are major structural components of bacterial membranes, and the ability to adapt the physical properties of membranes to changing environmental conditions is critical to bacterial survival (44–46). Due to the important biological function of lipids and evidence that arsenic can be incorporated in lipids, our study fills a significant gap in knowledge about As(V)'s impact on microbial lipidomes. A prior gas chromatography-MS (GC-MS) assessment of *A. tumefaciens* GW4 lipids by Wang et al. (6) focused only on the nature of the lipid chains and did not provide any information about headgroups for diacyl lipids. In contrast, the present study on *A. tumefaciens* strain GW4 utilized LC-MS, enabling the identification of five main glycerophospholipid classes (PC, PE, PG, PA, and PS), along with two minor lysophospholipids (lysoPE and lysoPC), whose levels are altered by As(V) (Table S2 and Table S3). The absence of cardiolipin in our lipid profile maybe due to the lipid extraction method used for this lipidomics analysis. Cardiolipin is generally found associated with membrane proteins and does not strongly partition with other lipids during chloroform-based lipid extraction (47). Decreased levels of PE are consistent with our data that ethanolamine levels are significantly lower in the As(V)-treated *A. tumefaciens* GW4 groups.

It is interesting to note that PC represents a significant fraction of the lipidome of *A. tumefaciens*, even though PC is more often associated with eukaryotic membranes. Only 10% of bacterial species produce PC; however, its presence in bacteria has been associated with important functions, including virulence and nitrogen fixation (48–50).

The specific role of PC in *A. tumefaciens* GW4 is unclear. Our LC-MS analysis reveals a mix of increases and decreases in abundance for different PC species, within the context of an overall decrease of phosphate incorporation in membrane components on exposure to As(V). Furthermore, three lipid species (PC 39:6, PC 38:6, and PC 35:1) were not detected in the As(V)-treated groups. These differences could be metabolically driven as part of arsenic resistance. Phosphatidylcholine can be hydrolyzed to release choline, from which betaine is generated, a metabolite that is found in higher levels in As(V)-treated GW4 cells, leading us to hypothesize that this mechanism is used to spare phosphate for other biological functions.

Our identification of lysophospholipids in *A. tumefaciens* strain GW4 was unexpected. There are reports of lysoPEs and lysoPGs being present in bacterial membranes (50). In mammals, lysoPC is formed as a result of the action of lecithin-cholesterol acyltransferase (LCAT) in plasma (51). Our finding of lysoPC 20:0 in GW4 (Fig. 7) is, to our knowledge, the first evidence of this lipid class in *A. tumefaciens*. The significant decrease of this lipid upon As(V) exposure suggests that lysoPC regulation is altered by As(V). LysoPCs are decreased in rats following arsenic exposure (52).

Under phosphate-limited conditions, bacteria have been shown to replace up to 40% of cellular P_i-containing compounds by (i) recycling phospholipids (53), (ii) downregulating genes encoding synthesis of P_i-rich techoic acids (54, 55), (iii) synthesizing and utilizing sulfolipids instead of phospholipids (56, 57), and (iv) replacing glycerophospholipids with glycerolipids (44). Evidence of P_i-sparing mechanisms being present in *A. tumefaciens* GW4 when grown in the presence of As(V) is revealed by the observed increase of deoxyadenosine and dAMP in this treatment group. Hydrolysis of dAMP releases orthophosphate, which can be used in molecules for which phosphate is critical (Table S1). It is quite possible that synthesis of arsenolipids is another mechanism of P_i sparing. Our previous work suggested that under low-phosphate conditions, arsenic accumulates in the lipid fraction along with a significant P_i decrease (12). Given that half of the glycerophospholipids in *A. tumefaciens* GW4 are decreased in abundance in the As(V)-treated group, our data strongly support a remodeling of lipid composition when *A. tumefaciens* GW4 is grown in the presence of As(V) (Table S2 and Table S3).

Beyond phosphate limitation, altering cellular lipid composition is an adaptation to different environmental conditions, including temperature, ionic strength, and antibiotics (47, 58–60). As described here, LC-MS omics-level analyses of bacterial metabolism can deepen our understanding of adaptive mechanisms and response to stress. Taken together, the metabolomics and lipidomics profiles obtained herein from LC-MS experiments enable us to better understand the cellular adaptations of *A. tumefaciens* strain GW4 to As(V) exposure and strengthen the relationship between changes in the biomolecular distribution of phosphate and cellular responses to arsenic.

MATERIALS AND METHODS

Materials and chemicals. $HNa_2AsO_4{\cdot}7H_2O$ [sodium arsenate, referred to here as As(V)], ammonium acetate, sodium chloride, formic acid, and all culture medium components were purchased from Sigma (St. Louis, MO). High-performance liquid chromatography (HPLC)-grade water, methanol, chloroform, acetonitrile, and acetone were purchased from Thermo-Fisher Scientific (Pittsburgh, PA). Pasteur pipettes, glass pipettes, and LC-MS autosampler vials were purchased from VWR (Radnor, PA). Screw-thread vials and 15-ml glass conical tubes were purchased from Thermo-Fisher Scientific (Pittsburgh, PA) and Corning (Pittston, PA), respectively.

Cell culture. *A. tumefaciens* GW4 was cultured at 30°C in 50 ml of defined minimal mannitol medium ($MMNH_4$) (61), modified to contain 100 μM P_i and 1 mM As(III), overnight. Cells were harvested by centrifugation for 20 min at 4,000 $\times$ *g*, washed 3 times with 20 ml of Tris buffer (pH 7.0), and resuspended in fresh $MMNH_4$ containing 100 μM P_i. Three of the six cultures were supplemented with 1 mM As(V). Culture conditions replicate those of Wang et al. and were designed to mimic low-P_i and increasing-As (V) conditions experienced by As(III)-oxidizing organisms in the environment (6). Cultures were monitored using optical density at 600 nm (OD_{600}) readings and harvested in late log phase (16 h). Cells were centrifuged at 12,000 rpm for 30 min and washed 3 times with 20 ml of ice-cold 0.85% NaCl, and resulting cell pellets were stored at −80°C until further use. Final biomass was assessed by measuring dry weight.

Metabolite extraction. Cell pellets were resuspended in 3 volumes of distilled water and sonicated for 5 min at a 60% duty cycle. An equal volume of methanol was added before vortexing for 30 s, followed by removal of cellular debris using centrifugation at 20,000 × *g* for 15 min at –4°C. To the supernatant solution, 5 volumes of cold acetone was added, and the resulting samples were frozen at –80°C overnight to precipitate proteins, which were subsequently removed by centrifugation at 20,000 × *g* for 5 min. For each sample, the resulting supernatant was transferred to a fresh Eppendorf tube and dried using a speed vacuum for 3 h (no heat), and the resulting final metabolite extracts were stored at –80°C until further analysis.

Lipid extraction. Lipids were extracted for LC-MS analysis following published protocols with slight modifications (62). For each sample, 0.01 to 0.012 g of cell pellet was resuspended in 0.45 ml of ice-cold 100 mM Tris buffer (pH 7.5) and transferred to a glass vial, followed by addition of 1.2 ml of 1:1 chloroform-methanol. After gentle mixing, the resulting mixture was centrifuged at 3,000 × *g* for 5 min. The lower (denser) chloroform layer containing the lipid fraction was carefully transferred into a clean glass vial using a glass Pasteur pipette. The procedure was repeated a second time, and the resulting lipid fractions were combined and dried under a stream of N_2. Samples were stored at –80°C until further analysis.

LC-MS analysis. LC-MS analysis was performed using an Agilent 1290 UPLC system connected to an Agilent 6538 quadrupole time of flight (Q-TOF) mass spectrometer (Agilent Technologies, Santa Clara, CA). A Cogent Diamond Hydride HILIC column (150 mm by 2.1 mm, 4 μm, 100 Å; Microsolv Technology Corporation, Eatontown, NJ), and a Zorbax RRHD Eclipse Plus (150 mm by 2.1 mm, 1.8 μm) reverse-phase C_{18} column (Agilent Technologies, Santa Clara, CA) were used to separate polar and nonpolar metabolites, respectively, prior to mass spectrometry (MS) analysis. Metabolite extracts were resuspended in 60 μl of 50% MeOH, from which 10 μl was injected into the C_{18} column for the nonpolar analysis. For analysis of polar compounds, metabolite extracts were diluted 10-fold before LC-MS on the HILIC column. The two mobile phases utilized for metabolite elution from the HILIC column consisted of A, H_2O, and B, acetonitrile, both containing 0.1% formic acid, with a flow rate of 0.6 ml min^{-1}. Gradient conditions for nonpolar metabolite elution from the C_{18} reverse-phase column were as follows. A gradient of A/B solvents starting at a 98:2 ratio was changed to 2:98 over 24 min, held at 2:98 for 2 min, and then returned to the starting condition for column equilibration (26.1 to 30 min). The gradient of A/B solvents (as described above) for elution of polar metabolites started at a ratio of 5:95, was ramped to 70:30 over 13 min, and returned to the 5:95 A/B solvent ratio for the remaining 1.5 min of the 15-min chromatography program. MS analysis was conducted in positive-ion mode with a capillary voltage of 3,500 V, a mass fragment voltage of 120 V, and a skimmer voltage of 45 V. The drying gas temperature was set at 350°C, with a flow of 12 liters/min and the nebulizer set to 55 lb/in^2. For the MS/MS experiment, a target list including previously determined exact masses and associated retention times was generated and used to guide the MS/MS fragmentation. The collision energy was fixed at 20 V across a 1.0-min retention time window.

For lipid analysis, the extracts were resuspended in 500 μl of methanol, transferred to 1.5-ml Eppendorf tubes, and speed vacuumed for 2 h. The resulting dried samples were resuspended in 150 μl of methanol and centrifuged at 10,000 rpm for 3 min to remove precipitates. Finally, 130 μl of each sample supernatant was transferred to LC-MS autosampler vials, and 2 μl was injected onto a C_8 Acquity UPLC bridged ethylene hybrid column (100- by 2.1-mm, inner diameter of 1.7 μm), at a flow rate of 0.6 ml min^{-1}. The mobile phase consisted of A, H_2O, and B, acetonitrile, both containing 0.1% formic acid. The gradient of A/B solvents started at 25% A and changed to 1% A over 15 min, remained at 1% for 13 min, then returned to initial conditions for the last 2 min of the LC run. MS analysis was conducted in positive- and negative-ion modes. For data-dependent MS/MS (the 3 most abundant ions), the scan range was set at 50 to 1,700 *m/z*, with an acquisition rate of 1 spectrum per second, with a collision energy of 10 V. Targeted MS/MS analyses were performed using collision energies of 10, 20, 30, and 40 V. Raw LC-MS data in the form of mass/charge ratio, retention time, and intensity are included in Data Set S1 in the supplemental material.

LC-MS data processing and statistical analysis. Data acquisition and spectral analysis were performed using the MassHunter software (Qualitative Analysis version B.04.00; Agilent Technologies). Raw data files were converted to MZxml format and processed by MZmine for peak detection to build chromatograms, retention time normalization, gap filling, and alignment. An intensity threshold of 1,000 was applied to discriminate signals (MS peaks) from noise. Retention time, mass/charge ratio (*m/z*), and spectral intensities normalized to cell pellet weight were tabulated. Statistical analyses, including principal-component analysis (PCA) and volcano plots, were generated using the Perseus software (63). Orthogonal partial least-squares discriminant analysis (OPLS-DA) was performed using MetaboAnalyst 4.0, and permutation tests of the OPLS-DA model were conducted to assess R2Y and Q2 values and robustness of the OPLS-DA modeling (64). To assign spectral features to specific metabolite identities (IDs), *m/z* values and retention time values were loaded into the Mummichog server with a mass tolerance of 20 ppm (65), and the presence of potential metabolites was further established using the BIOCYC reference database of genes and metabolic pathways for *Agrobacterium tumefaciens* CCNWGS0286, used as the reference organism. All *m/z* values detected from HILIC column eluants were cross-checked against our in-house metabolite standard library, with both observed *m/z* value and retention time required to match to metabolite standard values (*m/z* tolerance of 20 ppm and retention time tolerance of 0.5 min). Targeted MS/MS data were generated to further confirm metabolite IDs. MS/MS data were converted to "mgf" files using the ProteoWizard software, and MS/MS-based metabolite identification was performed using the SIRIUS and METLIN databases (66, 67). Pathway analysis was carried out using KEGG and MetaboAnalyst 4.0 (64, 68). Identification of lipid features was achieved using the LipidBlast and METLIN databases (15, 67).

TABLE 1 Primers used in this research

Primer pair	Primer sequence	Use
qRT-16S-F	5′ GGTATGGGCATTGGAGACGA 3′	qRT-PCR for 16S rRNA gene
qRT-16S-R	5′ GGCAACTAAGGGCGAGGG 3′	
qRT-mdh-F	5′ GTTTCCGCCTGTTCCTC 3′	qRT-PCR for *mdh*
qRT-mdh-R	5′ GTCAGCCAGCCCATCTT 3′	
qRT-SucDb-F	5′ AAGGGCGGCGTTCGTCT 3′	qRT-PCR for *sucD*b
qRT-SucDb-R	5′ TTCTCGGGCGTGTCGTG 3′	
qRT-SucDa-F	5′ CGGGCACGCTCACCTAT 3′	qRT-PCR for *sucD*a
qRT-SucDa-R	5′ CGCCGCATCTTCTTCA 3′	
qRT-fumC-F	5′ CATTTCCCGCTCGTCGTCT 3′	qRT-PCR for *fumC*
qRT-fumC-R	5′ GCTTCTTGGTGCCCATTTCG 3′	
qRT-sdhA-F	5′ ACCATCCATCGCTTTGCC 3′	qRT-PCR for *sdhA*
qRT-sdhA-R	5′ CGGTCGGGTGGAACTGAA 3′	

Quantitative RT-PCR analysis. Total cellular RNA extraction from harvested cells used the TRIzol reagent kit (Invitrogen, Grand Island, NY) following the manufacturer's instructions. Real-time reverse transcription-PCR (RT-PCR) was performed using an ABI VIIA7 in 0.1-ml Fast Optical 96-well reaction plates (ABI). Primers are listed in Table 1. Gene expression was normalized by threshold cycle ($\Delta\Delta C_T$) analysis with an iQ5 real-time PCR detection system (Bio-Rad, USA), and three technical and biological replicates were performed for each reaction. Statistically significant differences between control and treated samples were assessed using Student's *t* test, with *P* values of 0.01 to 0.05 considered borderline significant and *P* values of <0.01 considered statistically significant.

Analysis of ATP and NADH. Cells were collected by centrifugation (20,000 × *g*, 5 min, 4°C) and resuspended in 1 ml 0.4 M perchloric acid with 1.0 mM EDTA. After 5 min of ultrasonication on ice, cellular debris were removed by centrifugation (20,000 × *g*, 5 min, 4°C). Next, the pH of the extracts was adjusted to 7.0 using a 1 M K_2CO_3 stock solution and percolated through a 0.22-μm-pore filter membrane, and the resulting samples were analyzed by HPLC (HPLC 2690 series, Waters, MA). The mobile phase used to measure ATP and NADH contained 90% 50 mM phosphate buffer, 10% acetonitrile, and 3.22 g/liter tetrabutylammonium bromide (pH 6.8), at a flow of 1 ml/min. ATP and NADH were identified by comparing the retention times of the samples to that of authentic standards.

SUPPLEMENTAL MATERIAL

Supplemental material is available online only.

SUPPLEMENTAL FILE 1, PDF file, 0.9 MB.

SUPPLEMENTAL FILE 2, XLSX file, 0.9 MB.

ACKNOWLEDGMENTS

This research was supported in part by funding from the U.S. National Science Foundation to T.R.M. and B.B. (MCB 0817170 and MCB 1413321) and V.C. (MCB 1714556). W.Z. and G.W. receive support from the National Science Foundation of China (31670108) to G.W. Funding for the Proteomics, Metabolomics, and Mass Spectrometry Facility and the NMR Facility was made possible in part by the M. J. Murdock Charitable Trust, the National Science Foundation (DBI-1532078), and the National Institute of General Medical Sciences of the National Institutes of Health under award no. P20GM103474.

We thank Jesse Thomas for technical assistance with mass spectrometry.

We declare that we have no conflicts of interest.

REFERENCES

1. Andres J, Bertin PN. 2016. The microbial genomics of arsenic. FEMS Microbiol Rev 40:299–322. https://doi.org/10.1093/femsre/fuv050.
2. Kapaj S, Peterson H, Liber K, Bhattacharya P. 2006. Human health effects from chronic arsenic poisoning—a review. J Environ Sci Health A Tox Hazard Subst Environ Eng 41:2399–2428. https://doi.org/10.1080/10934520600873571.
3. Lloyd JR, Oremland RS. 2006. Microbial transformations of arsenic in the environment: from soda lakes to aquifers. Elements 2:85–90. https://doi.org/10.2113/gselements.2.2.85.
4. Vanden Hoven RN, Santini JM. 2004. Arsenite oxidation by the heterotroph *Hydrogenophaga* sp. str. NT-14: the arsenite oxidase and its physiological electron acceptor. Biochim Biophys Acta 1656:148–155. https://doi.org/10.1016/j.bbabio.2004.03.001.
5. Santini JM, Sly LI, Schnagl RD, Macy JM. 2000. A new chemolithoautotrophic arsenite-oxidizing bacterium isolated from a gold mine: phylogenetic, physiological, and preliminary biochemical studies. Appl Environ Microbiol 66:92–97. https://doi.org/10.1128/aem.66.1.92-97.2000.
6. Wang Q, Qin D, Zhang SZ, Wang L, Li JX, Rensing C, McDermott TR, Wang GJ. 2015. Fate of arsenate following arsenite oxidation in *Agrobacterium tumefaciens* GW4. Environ Microbiol 17:1926–1940. https://doi.org/10.1111/1462-2920.12465.

7. Dembitsky VM, Levitsky DO. 2004. Arsenolipids. Prog Lipid Res 43:403–448. https://doi.org/10.1016/j.plipres.2004.07.001.
8. Xue XM, Ye J, Raber G, Rosen BP, Francesconi KA, Xiong C, Zhu Z, Rensing C, Zhu YG. 2019. Identification of steps in the pathway of arsenosugar biosynthesis. Environ Sci Technol 53:634–641. https://doi.org/10.1021/acs.est.8b04389.
9. Rawle RA, Kang YS, Bothner B, Wang GJ, McDermott TR. 2019. Transcriptomics analysis defines global cellular response of *Agrobacterium tumefaciens* 5A to arsenite exposure regulated through the histidine kinases PhoR and AioS. Environ Microbiol 21:2659–2676. https://doi.org/10.1111/1462-2920.14577.
10. Shi KX, Li C, Rensing C, Dai X, Fan X, Wang GJ. 2018. Efflux transporter ArsK is responsible for bacterial resistance to arsenite, antimonite, trivalent roxarsone, and methylarsenite. Appl Environ Microbiol 84:e01842-18. https://doi.org/10.1128/AEM.01842-18.
11. Tokmina-Lukaszewska M, Shi ZJ, Tripet B, McDermott TR, Copié V, Bothner B, Wang GJ. 2017. Metabolic response of *Agrobacterium tumefaciens* 5A to arsenite. Environ Microbiol 19:710–721. https://doi.org/10.1111/1462-2920.13615.
12. Wang Q, Kang YS, Alowaifeer A, Shi KX, Fan X, Wang L, Jetter J, Bothner B, McDermott TR, Wang GJ. 2018. Phosphate starvation response controls genes required to synthesize the phosphate analog arsenate. Environ Microbiol 20:1782–1793. https://doi.org/10.1111/1462-2920.14108.
13. Rosen BP, Ajees AA, McDermott TR. 2011. Life and death with arsenic: arsenic life: an analysis of the recent report "A bacterium that can grow by using arsenic instead of phosphorus". Bioessays 33:350–357. https://doi.org/10.1002/bies.201100012.
14. Silva CAM, Graham B, Webb K, Ashton LV, Harton M, Luetkemeyer AF, Bokatzian S, Almubarak R, Mahapatra S, Hovind L, Kendall MA, Havlir D, Belisle JT, De Groote MA. 2019. A pilot metabolomics study of tuberculosis immune reconstitution inflammatory syndrome. Int J Infect Dis 84:30–38. https://doi.org/10.1016/j.ijid.2019.04.015.
15. Kind T, Liu KH, Lee DY, DeFelice B, Meissen JK, Fiehn O. 2013. LipidBlast in silico tandem mass spectrometry database for lipid identification. Nat Methods 10:755–758. https://doi.org/10.1038/nmeth.2551.
16. Cajka T, Fiehn O. 2017. LC-MS-based lipidomics and automated identification of lipids using the LipidBlast in-silico MS/MS library. Methods Mol Biol 1609:149–170. https://doi.org/10.1007/978-1-4939-6996-8_14.
17. Murphy RC, Axelsen PH. 2011. Mass spectrometric analysis of long-chain lipids. Mass Spectrom Rev 30:579–599. https://doi.org/10.1002/mas.20284.
18. Godzien J, Ciborowski M, Martínez-Alcázar MP, Samczuk P, Kretowski A, Barbas C. 2015. Rapid and reliable identification of phospholipids for untargeted metabolomics with LC-ESI-QTOF-MS/MS. J Proteome Res 14:3204–3216. https://doi.org/10.1021/acs.jproteome.5b00169.
19. Belfiore C, Ordoñez OF, Farías ME. 2013. Proteomic approach of adaptive response to arsenic stress in *Exiguobacterium* sp. S17, an extremophile strain isolated from a high-altitude Andean lake stromatolite. Extremophiles 17:421–431. https://doi.org/10.1007/s00792-013-0523-y.
20. Sacheti P, Patil R, Dube A, Bhonsle H, Thombre D, Marathe S, Vidhate R, Wagh P, Kulkarni M, Rapole S, Gade W. 2014. Proteomics of arsenic stress in the Gram-positive organism *Exiguobacterium* sp. PS NCIM 5463. Appl Microbiol Biotechnol 98:6761–6773. https://doi.org/10.1007/s00253-014-5873-6.
21. Ge Y, Ning Z, Wang Y, Zheng Y, Zhang C, Figeys D. 2016. Quantitative proteomic analysis of *Dunaliella salina* upon acute arsenate exposure. Chemosphere 145:112–118. https://doi.org/10.1016/j.chemosphere.2015.11.049.
22. Sanchez-Riego AM, Lopez-Maury L, Florencio FJ. 2014. Genomic responses to arsenic in the cyanobacterium *Synechocystis* sp. PCC 6803. PLoS One 9:e96826. https://doi.org/10.1371/journal.pone.0096826.
23. Halter D, Andres J, Plewniak F, Poulain J, Da Silva C, Arsène-Ploetze F, Bertin PN. 2015. Arsenic hyper tolerance in the protist *Euglena mutabilis* is mediated by specific transporters and functional integrity maintenance mechanisms. Environ Microbiol 17:1941–1949. https://doi.org/10.1111/1462-2920.12474.
24. Zhang Y, Chen S, Hao X, Su JQ, Xue X, Yan Y, Zhu YG, Ye J. 2016. Transcriptomic analysis reveals adaptive responses of an *Enterobacteriaceae* strain LSJC7 to arsenic exposure. Front Microbiol 7:636. https://doi.org/10.3389/fmicb.2016.00636.
25. Kashyap DR, Botero LM, Franck WL, Hassett DJ, McDermott TR. 2006. Complex regulation of arsenite oxidation in *Agrobacterium tumefaciens*. J Bacteriol 188:1081–1088. https://doi.org/10.1128/JB.188.3.1081-1088.2006.
26. Shi KX, Fan X, Qiao ZX, Han YS, McDermott TR, Wang Q, Wang GJ. 2017. Arsenite oxidation regulator AioR regulates bacterial chemotaxis towards arsenite in *Agrobacterium tumefaciens* GW4. Sci Rep 7:43252. https://doi.org/10.1038/srep43252.
27. Halliwell B, Whiteman M. 2004. Measuring reactive species and oxidative damage in vivo and in cell culture: how should you do it and what do the results mean? Br J Pharmacol 142:231–255. https://doi.org/10.1038/sj.bjp.0705776.
28. Flora SJ. 2011. Arsenic-induced oxidative stress and its reversibility. Free Radic Biol Med 51:257–281. https://doi.org/10.1016/j.freeradbiomed.2011.04.008.
29. Parvatiyar K, Alsabbagh EM, Ochsner UA, Stegemeyer MA, Smulian AG, Hwang SH, Jackson CR, McDermott TR, Hassett DJ. 2005. Global analysis of cellular factors and responses involved in *Pseudomonas aeruginosa* resistance to arsenite. J Bacteriol 187:4853–4864. https://doi.org/10.1128/JB.187.14.4853-4864.2005.
30. Cleiss-Arnold J, Koechler S, Proux C, Fardeau ML, Dillies MA, Coppee JY, Arsène-Ploetze F, Bertin PN. 2010. Temporal transcriptomic response during arsenic stress in *Herminiimonas arsenicoxydans*. BMC Genomics 11:709. https://doi.org/10.1186/1471-2164-11-709.
31. Li B, Lin J, Mi S, Lin J. 2010. Arsenic resistance operon structure in *Leptospirillum ferriphilum* and proteomic response to arsenic stress. Bioresour Technol 101:9811–9814. https://doi.org/10.1016/j.biortech.2010.07.043.
32. Sies H. 1999. Glutathione and its role in cellular functions. Free Radic Biol Med 27:916–921. https://doi.org/10.1016/s0891-5849(99)00177-x.
33. Thompson BC, Halliday GM, Damian DL. 2015. Nicotinamide enhances repair of arsenic and ultraviolet radiation-induced DNA damage in HaCaT keratinocytes and ex vivo human skin. PLoS One 10:e0117491. https://doi.org/10.1371/journal.pone.0117491.
34. Zhang LS, Davies SS. 2016. Microbial metabolism of dietary components to bioactive metabolites: opportunities for new therapeutic interventions. Genome Med 8:46. https://doi.org/10.1186/s13073-016-0296-x.
35. Zoghlami LB, Djebali W, Abbes Z, Hediji H, Maucourt M, Moing A, Brouquisse R, Chaïbi W. 2011. Metabolite modifications in *Solanum lycopersicum* roots and leaves under cadmium stress. Afr J Biotechnol 10:567–579. http://www.academicjournals.org/AJB.
36. Arora N, Dubey D, Sharma M, Patel A, Guleria A, Pruthi PA, Kumar D, Pruthi V, Poluri KM. 2018. NMR-based metabolomic approach to elucidate the differential cellular responses during mitigation of arsenic(III, V) in a green microalga. ACS Omega 3:11847–11856. https://doi.org/10.1021/acsomega.8b01692.
37. Zou H, Chen N, Shi M, Xian M, Song Y, Liu J. 2016. The metabolism and biotechnological application of betaine in microorganism. Appl Microbiol Biotechnol 100:3865–3876. https://doi.org/10.1007/s00253-016-7462-3.
38. Kalia K, Flora SJ. 2005. Strategies for safe and effective therapeutic measures for chronic arsenic and lead poisoning. J Occup Health 47:1–21. https://doi.org/10.1539/joh.47.1.
39. Mittenhuber G. 2001. Phylogenetic analyses and comparative genomics of vitamin B6 (pyridoxine) and pyridoxal phosphate biosynthesis pathways. J Mol Microbiol Biotechnol 3:1–20.
40. Dalto D, Matte JJ. 2017. Pyridoxine (vitamin B6) and the glutathione peroxidase system; a link between one-carbon metabolism and antioxidation. Nutrients 9:189. https://doi.org/10.3390/nu9030189.
41. Bergquist ER, Fischer RJ, Sugden KD, Martin BD. 2009. Inhibition by methylated organoarsenicals of the respiratory 2-oxo-acid dehydrogenases. J Organomet Chem 694:973–980. https://doi.org/10.1016/j.jorganchem.2008.12.028.
42. Afzal MI, Delaunay S, Paris C, Borges F, Revol-Junelles AM, Cailliez-Grimal C. 2012. Identification of metabolic pathways involved in the biosynthesis of flavor compound 3-methylbutanal from leucine catabolism by *Carnobacterium maltaromaticum* LMA 28. Int J Food Microbiol 157:332–339. https://doi.org/10.1016/j.ijfoodmicro.2012.05.010.
43. Chen W, Taylor NL, Chi Y, Millar AH, Lambers H, Finnegan PM. 2014. The metabolic acclimation of *Arabidopsis thaliana* to arsenate is sensitized by the loss of mitochondrial lipoamide dehydrogenase 2, a key enzyme in oxidative metabolism. Plant Cell Environ 37:684–695. https://doi.org/10.1111/pce.12187.
44. Hölzl G, Dörmann P. 2007. Structure and function of glycoglycerolipids in plants and bacteria. Prog Lipid Res 46:225–243. https://doi.org/10.1016/j.plipres.2007.05.001.
45. Sohlenkamp C, Geiger O. 2016. Bacterial membrane lipids: diversity in structures and pathways. FEMS Microbiol Rev 40:133–159. https://doi.org/10.1093/femsre/fuv008.
46. Slavetinsky C, Kuhn S, Peschel A. 2017. Bacterial aminoacyl phospholipids—biosynthesis and role in basic cellular processes and pathogenicity.

Biochim Biophys Acta Mol Cell Biol Lipids 1862:1310–1318. https://doi.org/10.1016/j.bbalip.2016.11.013.
47. Lopalco P, Angelini R, Lobasso S, Köcher S, Thompson M, Müller V, Corcelli A. 2013. Adjusting membrane lipids under salt stress: the case of the moderate halophilic organism *Halobacillus halophilus*. Environ Microbiol 15:1078–1087. https://doi.org/10.1111/j.1462-2920.2012.02870.x.
48. Conde-Alvarez R, Grilló MJ, Salcedo SP, De Miguel MJ, Fugier E, Gorvel JP, Moriyón I, Iriarte M. 2006. Synthesis of phosphatidylcholine, a typical eukaryotic phospholipid, is necessary for full virulence of the intracellular bacterial parasite *Brucella abortus*. Cell Microbiol 8:1322–1335. https://doi.org/10.1111/j.1462-5822.2006.00712.x.
49. Geiger O, López-Lara IM, Sohlenkamp C. 2013. Phosphatidylcholine biosynthesis and function in bacteria. Biochim Biophys Acta 1831:503–513. https://doi.org/10.1016/j.bbalip.2012.08.009.
50. Kondakova T, Merlet-Machour N, Chapelle M, Preterre D, Dionnet F, Feuilloley M, Orange N, Duclairoir-Poc C. 2015. A new study of the bacterial lipidome: HPTLC-MALDI-TOF imaging enlightening the presence of phosphatidylcholine in airborne *Pseudomonas fluorescens* MFAF76a. Res Microbiol 166:1–8. https://doi.org/10.1016/j.resmic.2014.11.003.
51. Kougias P, Chai H, Lin PH, Lumsden AB, Yao Q, Chen C. 2006. Lysophosphatidylcholine and secretory phospholipase A2 in vascular disease: mediators of endothelial dysfunction and atherosclerosis. Med Sci Monit 12:RA5–RA16.
52. Rivas-Santiago C, González-Curiel I, Zarazua S, Murgu M, Cardona AR, Lazalde B, Lara-Ramírez EE, Vázquez E, Castañeda-Delgado JE, Rivas-Santiago B, Adrián Lopez J, Cervantes-Villagrana AR, López-Hernández Y. 2019. Lipid metabolism alterations in a rat model of chronic and intergenerational exposure to arsenic. Biomed Res Int 2019:4978018. https://doi.org/10.1155/2019/4978018.
53. Geiger O, Röhrs V, Weissenmayer B, Finan TM, Thomas-Oates JE. 1999. The regulator gene *phoB* mediates phosphate stress-controlled synthesis of the membrane lipid diacylglyceryl-N,N,N-trimethylhomoserine in *Rhizobium* (*Sinorhizobium*) *meliloti*. Mol Microbiol 32:63–73. https://doi.org/10.1046/j.1365-2958.1999.01325.x.
54. Lang WK, Glassey K, Archibald AR. 1982. Influence of phosphate supply on teichoic acid and teichuronic acid content of *Bacillus subtilis* cell walls. J Bacteriol 151:367–375. https://doi.org/10.1128/JB.151.1.367-375.1982.
55. Salzberg LI, Botella E, Hokamp K, Antelmann H, Maaß S, Becher D, Noone D, Devine KM. 2015. Genome-wide analysis of phosphorylated PhoP binding to chromosomal DNA reveals several novel features of the PhoPR-mediated phosphate limitation response in *Bacillus subtilis*. J Bacteriol 197:1492–1506. https://doi.org/10.1128/JB.02570-14.
56. Souza V, Eguiarte LE, Siefert J, Elser JJ. 2008. Microbial endemism: does phosphorus limitation enhance speciation? Nat Rev Microbiol 6:559–564. https://doi.org/10.1038/nrmicro1917.
57. Zavaleta-Pastor M, Sohlenkamp C, Gao JL, Guan Z, Zaheer R, Finan TM, Raetz CRH, López-Lara IM, Geiger O. 2010. *Sinorhizobium meliloti* phospholipase C required for lipid remodeling during phosphorus limitation. Proc Natl Acad Sci U S A 107:302–307. https://doi.org/10.1073/pnas.0912930107.
58. Zhang YM, Rock CO. 2008. Membrane lipid homeostasis in bacteria. Nat Rev Microbiol 6:222–233. https://doi.org/10.1038/nrmicro1839.
59. Schenk ER, Nau F, Thompson CJ, Tse-Dinh YC, Fernandez-Lima F. 2015. Changes in lipid distribution in *E. coli* strains in response to norfloxacin. J Mass Spectrom 50:88–94. https://doi.org/10.1002/jms.3500.
60. Rashid R, Cazenave-Gassiot A, Gao IH, Nair ZJ, Kumar JK, Gao L, Kline KA, Wenk MR. 2017. Comprehensive analysis of phospholipids and glycolipids in the opportunistic pathogen *Enterococcus faecalis*. PLoS One 12:e0175886. https://doi.org/10.1371/journal.pone.0175886.
61. Somerville JE, Kahn ML. 1983. Cloning of the glutamine synthetase I gene from *Rhizobium meliloti*. J Bacteriol 156:168–176. https://doi.org/10.1128/JB.156.1.168-176.1983.
62. Folch J, Lees M, Stanley GS. 1957. A simple method for the isolation and purification of total lipids from animal tissues. J Biol Chem 226:497–509.
63. Tyanova S, Temu T, Sinitcyn P, Carlson A, Hein MY, Geiger T, Mann M, Cox J. 2016. The Perseus computational platform for comprehensive analysis of (prote)omics data. Nat Methods 13:731–740. https://doi.org/10.1038/nmeth.3901.
64. Chong J, Soufan O, Li C, Caraus I, Li S, Bourque G, Wishart DS, Xia JG. 2018. MetaboAnalyst 4.0: towards more transparent and integrative metabolomics analysis. Nucleic Acids Res 46:W486–W494. https://doi.org/10.1093/nar/gky310.
65. Li S, Park Y, Duraisingham S, Strobel FH, Khan N, Soltow QA, Jones DP, Pulendran B. 2013. Predicting network activity from high throughput metabolomics. PLoS Comput Biol 9:e1003123. https://doi.org/10.1371/journal.pcbi.1003123.
66. Bocker S, Letzel MC, Liptak Z, Pervukhin A. 2009. SIRIUS: decomposing isotope patterns for metabolite identification. Bioinformatics 25:218–224. https://doi.org/10.1093/bioinformatics/btn603.
67. Tautenhahn R, Cho K, Uritboonthai W, Zhu Z, Patti GJ, Siuzdak G. 2012. An accelerated workflow for untargeted metabolomics using the METLIN database. Nat Biotechnol 30:826–828. https://doi.org/10.1038/nbt.2348.
68. Kanehisa M, Goto S, Sato Y, Kawashima M, Furumichi M, Tanabe M. 2014. Data, information, knowledge and principle: back to metabolism in KEGG. Nucleic Acids Res 42:D199–D205. https://doi.org/10.1093/nar/gkt1076.